DESIGN OF MAIN PROPULSION SYSTEM FOR A REUSABLE SUBORBITAL ROCKET

Fraser McRoberts
University of Strathclyde, United Kingdom, fraser.mcroberts.2013@uni.strath.ac.uk

Callum Harrower
University of Strathclyde, United Kingdom, callum.harrower.2013@uni.strath.ac.uk
Blair Hutchison
University of Strathclyde, United Kingdom, blair.hutchison.2013@uni.strath.ac.uk
Wai Get Law
University of Strathclyde, United Kingdom, wai.law.2013@uni.strath.ac.uk
Ciara McGrath
University of Strathclyde, United Kingdom, ciara.mcgrath.2013@uni.strath.ac.uk
Frazer McLean
University of Strathclyde, United Kingdom, frazer.mclean.2013@uni.strath.ac.uk

In recent years there has been an increased interest in the use of CubeSats to perform research in the realms of microgravity and earth observation. Previously, CubeSats have generally been placed into orbit as secondary payloads, piggy-backing on the launches of larger spacecraft. This has meant that CubeSat orbits and launch schedules have been decided by the requirements of other missions, restricting the manner in which they can be used. Due to the lack of flexibility in mission design afforded by traditional launch options, and the increasing competition for CubeSat launch spots, it has become desirable to develop a dedicated small satellite launch platform. This would allow for the execution of more novel and exciting missions, utilising orbits specifically designed with small satellites in mind. Tranquility Aerospace Ltd are currently engaged in the design of a two-stage vertical take-off and landing (VTVL) launcher, aimed at the small satellite market. Due to the many engineering challenges involved, they are aiming to first develop a suborbital launch vehicle in order to test the technologies necessary. This launch vehicle will be single-stage, and capable of vertical take-off and landing. As a student project at the University of Strathclyde, the main rocket propulsion system for this vehicle is being designed. This paper will outline the development of the propulsion system, including the propellant feed system, injector plate, thrust chamber and thermal control system. The key design driver is to lower the overall system mass, including the mass of the propellant. Comparisons of the impact of different subsystem configurations on performance will be assessed and discussed, and a focus will be placed on aspects of the design impacted by the requirement for reusability. The goal is to produce a fully workable design which is ready for manufacture and can be taken forward to the testing phase of development.

I. INTRODUCTION

Typical launch vehicles are single-use, have no requirement for a controlled descent, and carry payloads on the order of several tons. The vehicle being developed by Tranquility Aerospace Ltd is to be fully reusable, capable of vertical take-off and landing, and will only carry payloads on the order of a few kilograms.

Although the payloads are small, the requirement for the vehicle to both reach a high altitude and perform a controlled descent mean that the engine must be designed to be as efficient as possible.

The design of the engine is split into five main components: the propellant feed system; the injection system; the combustion chamber; the nozzle; and the thermal control system. At each stage a conventional design approach was followed initially, and consideration was then given to how this could be

Property	Value	
Launch Mass	400	kg
Dry Mass	80	kg
Thrust (Take-off)	5000	N
Thrust (Landing)	800	N
Chamber Pressure	50	bar
Fuel	Kerosene (RP-1)	
Oxidiser	Hydrogen Peroxide (95% H_2O_2 + 5% H_2O)	

Table 1: Target specifications for launch vehicle.

altered to improve the performance of the engine given its unique requirements.

The target specifications for the launch vehicle are given in Table 1.

II. METHOD
II.I Propellant Feed System
In a liquid rocket engine, the propellants are combusted in a highly pressurised state, in order to maximise the efficiency of combustion. As a result, either the propellants must be pressurised on the ground and stored in high-pressure tanks, or pumps must be included on board in order to pressurise them immediately before combustion.

Both a pressure-fed and a pump-fed system are compared in terms of system mass required to provide the desired chamber pressure.

II.I.I Pressure Fed System
The pressure-fed system analysed is a regulated gas system. In this system a tank of high pressure gas is stored above the pressurised propellant tanks. When the propellant is required, the gas is allowed to enter the propellant tanks, forcing the propellant out. This allows for a constant pressure and flow rate of propellants to the engine.

The mass of the system can be estimated as the mass of the high-pressure propellant tanks, the mass of the high-pressure gas tank, and the mass of the high pressure gas. The masses of the high pressure tanks can be calculated using eq. [1] (assuming they are cylindrical), while the mass of the high pressure gas can be calculated using eq. [2].

$$M = 2\pi r^2 (r+h) p \frac{\rho}{\sigma_y} \qquad [1]$$

$$m_0 = \frac{p_p V_p}{R T_0} \left[\frac{\gamma}{1 - \frac{p_r}{p_0}} \right] \qquad [2]$$

II.I.II Pump Fed System
The pump-fed system analysed consists of two unpressurised propellant tanks, and two centrifugal pumps. In order to power the pumps, a small portion of the hydrogen peroxide flow is diverted and decomposed over a catalyst bed into a hot gas, which is then run over a turbine.

The power required to run each of the pumps can be calculated using eq. [3].

$$P_{\text{pump}} = \frac{\dot{m}(p_{\text{out}} - p_{\text{in}})}{\eta_{\text{pump}} \rho} \qquad [3]$$

The pump powers can then be summed together to find the required turbine power. Assuming the turbine exhausts to atmospheric pressure, the mass flow rate required through the turbine can be calculated using eq. [4].

$$\dot{m}_{gg} = \frac{P_{\text{turbine}}}{C_p T_{\text{in}} \eta_{\text{turbine}} \left(1 - \left(\frac{p_{\text{in}}}{p_{\text{out}}} \right)^{\frac{1-\gamma}{\gamma}} \right)} \qquad [4]$$

Using knowledge of the required power, pressure ratios and flow rates for the various pieces of turbo machinery, masses were estimated based on existing designs. Combining these with the masses of the unpressurised tanks (calculated using eq. [1]), and the mass of oxidiser required to run the turbine throughout the flight, allows an overall mass estimate to be constructed for the pump-fed system. Note that for all turbo machinery, efficiencies were taken as 80%.

II.I.III Losses
In reality there will be losses in the system connecting the pumps to the combustion chamber. The actual pressures that will have to be produced in order to get the propellants to the chamber can be found using eq. [5] and eq. [6].

$$p_{\text{fuel pump,exit}} = p_{\text{chamber}} + \Delta p_{\text{inj,fuel}}$$
$$+ \Delta p_{\text{f,fuel}} + \Delta p_{\text{V,fuel}} \qquad [5]$$

$$p_{\text{ox,pump,exit}} = p_{\text{chamber}} + \Delta p_{\text{inj,ox}} + \Delta p_{\text{f,ox}}$$
$$+ \Delta p_{\text{V,ox}} + \Delta p_{\text{cool,ox}} \qquad [6]$$

The pressure drop over the injector for both of the propellants is calculated as part of the injector plate design outlined in section II.II.

Friction losses are determined by means of a friction factor, calculated based on the Reynolds number of the fluid as well as the pipe relative roughness. The Reynolds number is calculated for each section of the piping using eq. [7]. The friction factor is then found by iteratively solving the Colebrook equation shown in eq. [8]. The pressure loss can then be calculated using eq. [9].

$$\text{Re} = \frac{\rho u_f D}{\mu} \qquad [7]$$

$$\frac{1}{\sqrt{f}} = -2 \log_{10} \left(\frac{\varepsilon}{3.7D} + \frac{2.51}{\text{Re}\sqrt{f}} \right) \qquad [8]$$

$$\Delta P_f = \rho f \frac{L}{D} \frac{u_f^2}{2} \qquad [9]$$

In order to determine the pressure drop across a valve eq. [9] is considered once more, with an equivalent length being used corresponding to the type of valve being analysed.

The regenerative cooling losses were calculated by examining the frictional losses that would be incurred in each of the narrow cooling channels. These losses were calculated in a similar manner to the frictional losses in the piping.

II.II Injection System

At the end of the feed system, the oxidiser passes over a catalyst pack. This causes the hydrogen peroxide to decompose into gaseous mixture of superheated steam and oxygen, and experience an increase in temperature to approximately 1173 K. When the liquid kerosene makes contact with this mixture, it auto-ignites, forgoing the requirement for any ignition system. The purpose of the injection system in this case then, is to introduce the propellants into the engine in a manner which ensures efficient mixing and combustion.

The injection system in this engine takes the form of an orifice plate. The products of the hydrogen peroxide decomposition are allowed to flow directly up to the plate, while the kerosene is directed through a series of manifolds to reach its specific orifices. Eq. [10] shows the relationship between the size of the orifices, the velocity at the chamber inlet, and the pressure drop across the plate.

$$ v = \frac{Q}{A} = C_d \sqrt{\frac{2\Delta p}{\rho}} \qquad [10] $$

In order to calculate the appropriate properties for the oxidiser as it enters the combustion chamber, the decomposition process must be analysed. The decomposition of hydrogen peroxide is given by eq. [11].

$$ 2H_2O_2 \rightarrow 2H_2O + O_2 \qquad [11] $$
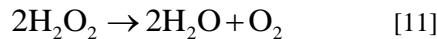
Using the atomic weights of hydrogen and oxygen, the mass percentages of the superheated steam and oxygen in the decomposed mixture can be determined, and therefore the density of the final fluid can be calculated using the general rule of mixtures.

II.II.I Atomisation Quality

As the oxidiser is decomposed before entering the combustion chamber, the mixing process occurs as a spray of liquid kerosene across a cloud of steam and gaseous oxygen. It is desirable to have as fine a spray

as possible, as this will result in a higher total surface area of kerosene, and more efficient combustion.

The fineness of a spray can be represented by its Sauter Mean Diameter. This is the diameter of a particle with the same volume to surface area ratio as the entire spray. Semiao et al.[12] gives an expression for calculating the Sauter Mean Diameter for airblast injectors as in eq. [12].

$$ \text{SMD} = 1.58 \times 10^3 \left[\frac{\sigma}{\rho_{\text{ox}} u_{\text{ox}}^2 d_0} \right]^{0.5} d_0 \left[\frac{\sigma}{\mu_{\text{fuel}} u_{\text{ox}}} \right]^{0.55} $$

$$ \times \left(\frac{\rho_{\text{ox}}}{\rho_{\text{fuel}}} \right) \left[1 + \frac{1}{\text{OFR}} \right]^{0.5} + 166 \left[\frac{\mu_{\text{fuel}}}{\rho_{\text{fuel}} d_0 u_{\text{ox}}} \right]^{1.1} $$

$$ \times \left[\frac{s}{\rho_{\text{ox}} u_{\text{ox}}^2 d_0} \right]^{0.2} \times d_0 \left(\frac{\rho_{\text{fuel}}}{\rho_{\text{ox}}} \right)^{0.35} \left[1 + \frac{1}{\text{OFR}} \right]^{-0.48} $$

$$ [12] $$

In order to reduce the Sauter Mean Diameter of the spray, the orifices in the injection plate are sized such that the fuel orifices are as small as possible, and there is a large difference in velocity between the two propellants.

II.II.II Spray Pattern

The placement of the orifices on the injector plate also has an impact on the mixing of the propellants and combustion efficiency. Three different orifice patterns were created and then simulated in a CFD model, the development of which is detailed by Harrower[3]. These orifice patterns tested are shown in Figure 1.
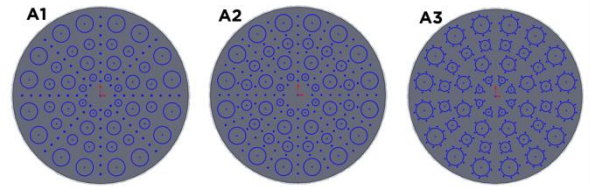

Figure 1: Diagram of various orifice patterns considered.

Injector A1 uses a similar layout as used by Jo et al.[4] for a comparable hydrogen peroxide/kerosene system. Injector A2 is a variation on this design which distributes more fuel orifices in between the arrangement of oxidiser inlets, in order to encourage better mixing and avoid unburnt volumes of fuel and oxidiser. Injector A3 draws inspiration from the Bristol Siddeley Gamma rocket engines documented by Andrews and Sunley[2], moving the fuel orifices to the immediate circumference of the oxidiser inlets, in

order to produce a more immediate mixing between the two.

II.III Combustion Chamber

In order to find the conditions in the combustion chamber, an analytical model of the combustion process was considered.

Using the method described in section II.II on the injection system, the molecular weight of the propellant components can be used to find the mass fractions of the resulting mixture after catalytic decomposition. These can then be used in the combustion model.

On passing through the catalyst these components heat up to 1173 K, allowing a full picture of the combustion conditions to be obtained as shown in Table 2.

		Mass fraction (%)	Temperature (K)
Fuel	RP-1	100	298
Oxidiser	H_2O	55.3	1173
	O_2	44.7	1173

Table 2: Propellant conditions for combustion.

The combustion chamber pressure, p_1, is specified as 50 bar, and the oxidiser to fuel ratio (OFR) chosen is 7.35. These parameters were used in NASA's Chemical Equilibrium Applications (CEA) to model the combustion and calculate the resulting components and their states. The output from CEA indicates the properties of the flow into the nozzle are:

$$\gamma = 1.1291$$
$$R = 376.373 \text{ J/kgK}$$
$$T_1 = 2877.8 \text{ K}$$

II.III.I Combustion Chamber Geometry

The combustion chamber volume can be calculated by considering eq. [13], based on the throat area (A_t).

$$V_{\text{chamber}} = L^* A_t \qquad [13]$$

In order to determine the appropriate value of characteristic length (L^*) to use, as well as what the diameter of the combustion chamber should be, various options were tested in a CFD model, the development of which is detailed by Harrower[3].

In the contraction region, the combustion exhaust gases must be able to flow optimally to the throat; therefore the convergent angle cannot be steep. An angle of 60° is often suggested in the literature[11]. A

Bezier curve was fitted to the convergent section such that the steepest wall angle did not exceed 60°.

The volume of revolution of the Bezier curve was determined, and used to calculate an additional length to be added to the combustion chamber as to preserve the correct total volume.

II.IV Nozzle

The purpose of the nozzle is to simultaneously expand and accelerate the flow produced by the combustion of gases in the combustion chamber. For typical chemical propulsion, the measured performance of a real rocket is from 1 to 6 % below the ideal performance[11]. For this reason, it is accepted practice to design a nozzle using ideal parameters, later applying correction factors to predict real performance.

II.IV.I Thrust Chamber Conditions

The combustion chamber acts as the convergent part of the convergent-divergent nozzle, and therefore sets the inlet conditions required for the isentropic flow equations.
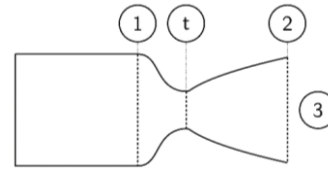

Figure 2: Diagram of the areas of the thrust chamber and the associated symbol subscripts. For example, v_2 is the exit velocity and p_1 is the chamber pressure. Region 3 corresponds to the local atmospheric conditions.

The thrust provided by the nozzle is produced by the flow rate of the exhaust, and a pressure difference at the nozzle exit as shown in eq. [14].

$$F = \eta_T \dot{m} v_2 + (p_2 - p_3) A_2 \qquad [14]$$

At the design condition, $p_2 = p_3$, simplifying the equation. The exhaust velocity is given by eq. [15], and is shown to be a function of the chamber conditions $(\gamma, R, T_1, p_1, v_1)$ and the exit condition (p_2).

$$v_2 = \sqrt{\frac{2\gamma}{\gamma - 1} RT_1 \left[1 - \left(\frac{p_2}{p_1} \right)^{\frac{\gamma-1}{\gamma}} \right] + v_1^2} \qquad [15]$$

Assuming negligible chamber velocity, the exit pressure at the design condition can be used to find the exit velocity.

The required mass flow rate is then found by rearranging the simplified form of eq. [14] for $\dot{m}$, but in order to quantify the thrust efficiency (η_t), the nozzle shape must be chosen as in II.IV.III.

Once a mass flow rate has been calculated, the throat and exit area are found using the mass continuity eq. [16] with known values for $\dot{m}$ and v. The fluid density, ρ, is calculated using eq. [17] and eq. [18] [11].

$$A = \frac{\dot{m}}{\rho v} \quad [16]$$

$$\rho_t = \rho_1 \left(\frac{\gamma + 1}{2} \right)^{\frac{1}{1-\gamma}} \quad [17]$$

$$\rho_2 = \rho_1 \left(\frac{p_2}{p_1} \right)^{\frac{1}{\gamma}} \quad [18]$$

II.IV.II Optimal Expansion

For a given design condition, the exit pressure is fixed, yet the atmospheric pressure changes with altitude. For this reason the nozzle is most efficient at the design condition.

When the external pressure is greater than the exit pressure, the flow is said to be over-expanded and constricts upon leaving the nozzle.

If the exit pressure is below a certain threshold— typically 25 to 40 % of atmospheric pressure[11] —the pressure difference is too great and the flow constriction starts inside the nozzle as flow separates from the nozzle wall. This reduces the thrust produced by the engine.

If the external pressure is less than the exit pressure (such as operation in a vacuum), this is known as under-expanded flow and the flow swells upon leaving the nozzle.

It is clear that both under- and over-expanded flow are not optimal, and so the design condition should be chosen to reduce the losses overall. Anecdotally, it is not uncommon for nozzle configurations to be slightly over-expanded at launch.

In order to find the optimum configuration for the engine being developed, a trajectory simulation of different nozzle design conditions was created, recording the total propellant usage for each design altitude.

During descent and landing, the atmospheric pressure alone is not considered to be enough to determine the back pressure, as the engine is facing the flow. Instead, the stagnation pressure of the high velocity air being forced toward the engine is calculated. This could mean that a nozzle with low design exit pressure may not be able to be used, as the increase in back pressure during landing could cause flow separation.

II.IV.III Nozzle Geometry

With an exit pressure chosen, the throat and exit areas are fixed, however there remains the question of which shape to use in between. A 'reference' 15° half angle conic nozzle is often used initially, giving a baseline length.
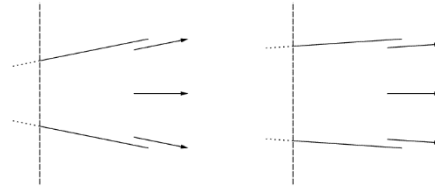

Figure 3: Cut-off exit of two different conic nozzles. Arrows depict exit flow angle.

There are conflicting demands on nozzle geometry: shorter nozzles have less mass and thus contribute to the efficiency of the engine; but longer nozzles have more uniform flow at the exit, as shown in Figure 3. This is important as any transverse flow does not contribute to the thrust. This can be calculated as an efficiency term, as shown in eq. [19], where α is the angle of the wall at the exit.

$$\lambda = \frac{1}{2}(1 + \cos\alpha) \quad [19]$$

If the nozzle wall is too steep, the flow will separate from the wall and fail to expand as it should. This could occur in a conic nozzle that is too short, but also in a nozzle with curved walls.

Dr. G.V.R. Rao calculated equations for the optimal bell nozzle[8]. The nozzle is comprised of convergent, divergent, and parabolic arcs, as shown in Figure 4. θ_1 is chosen such that the convergent arc meets the combustion chamber geometry's convergent section.
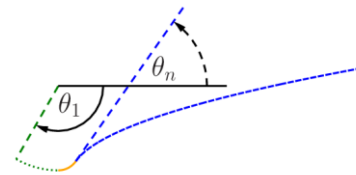

Figure 4: Rao optimal bell nozzle, with each constituent curve styled differently. Note that θ_1 and θ_n are relative to a line parallel to the nozzle axis.

In order to determine the maximum allowable inflection angle ($\theta_{n,max}$), the Prandtl-Meyer expansion angle is calculated using eq. [20] for the nozzle exit Mach number.

$$v = \sqrt{\frac{\gamma+1}{\gamma-1}} \arctan \sqrt{\frac{\gamma-1}{\gamma+1}(\mathrm{Ma}_2{}^2 - 1)} - \arctan \sqrt{\mathrm{Ma}_2{}^2 - 1} \quad [20]$$

$$\theta_{n,\max} = \frac{v}{2} \quad [21]$$

II.IV.IV Thrust Losses

Thrust losses are estimated from empirical data[11]. Small diameter chambers have associated losses due to an undersized contraction region (or lack thereof). Chamber to throat area ratios greater than nine have negligible losses.

The interaction of the boundary layer and wall friction typically reduces the exhaust velocity by 0.5 to 1 %, but "seldom exceeds 1 %"[11]. This loss increases as the nozzle length and area ratio increase, which should be taken into account if a design altitude of greater than sea level is used.

Particles or droplets in the gas can cause losses of up to 5 %, as they do not expand with the flow in the nozzle. As there are no additives in the propellant used, particles are not a concern. Only the fuel enters the chamber as a liquid, but due to the chamber conditions all fuel should evaporate before reaching the nozzle. Nevertheless, a loss of 2 % is assumed as a safety factor.

It is known that the combustion process is not steady, with oscillating flow accounting for a small loss. Chemical reactions in the nozzle change the gas properties such that a loss of typically 0.5 % occurs. The composition of the nozzle gases is assumed to be at equilibrium, however this overestimates the performance by 1 to 4 %, which must be accounted for. Non-uniform gas composition leftover from combustion can reduce performance. All combustion effects considered, a loss of 5 to 10 % is assumed.

Combining these losses yields a total thrust efficiency (η_t) of 86 to 91 %.

II.IV.V Throttling

A rocket engine is usually throttled by reducing the mass flow rate of the propellants. A nozzle designed for full throttle has a fixed shape, and thus calculating the effect on thrust is complex.

$$F = f(\dot{m}, v_2) \quad [22]$$

$$v_2 = f(\gamma, R, T_1, p_1, p_2) \quad [23]$$

The parameters that affect thrust can be determined from eqs. [22] and [23]. Note that without changing the propellant, and considering that p_2 is a result of the nozzle shape conditions, only the chamber conditions p_1 and T_1 can be varied. Alternatively, the propellant properties could be altered. This means there are three different throttling methods to consider.

Standard propellant: This method uses the propellant at the optimal oxidiser-to-fuel ratio as used for full throttle but with a reduced overall mass flow rate. The advantage of using this method is that the feed system would only be required to provide a fixed OFR.

Oxidiser only: In this case no fuel is used and so no combustion occurs. Instead the oxidiser is decomposed over the catalyst and passed through the nozzle in a similar manner to a standard monopropellant engine. This method was theorised to allow a lower thrust range due to lack of combustion with fuel in the chamber, but may not be feasible given the vastly different chamber conditions.

Variable oxidiser to fuel ratio: A parametric study of the OFR was carried out, and the results examined using CEA. For the optimal OFR, $\gamma = 1.1291$ as in section II.III. It was found that for OFR values above and below 7.35, the exhaust heat capacity ratio would increase up to ≈ 1.25, which is the heat capacity ratio for the fuel.

As the propellant mass flow rate is reduced, the chamber pressure varies linearly. It then follows that the nozzle exit pressure decreases as the chamber pressure is reduced. As mentioned previously, back pressures that are too low can cause flow separation in the nozzle. During landing, the maximum allowable back pressure is then dependent on the throttled mass flow rate.

II.V Thermal Control System

As the exhaust gases exit the engine, the materials used to fabricate the thrust chamber are exposed to very high temperatures. In order to avoid engine failure, these materials must be cooled and kept within reasonable temperature limits.

Two options are investigated. The first option is a conventional regenerative cooling system, in which the oxidiser is passed around the outside of the chamber before being combusted, serving to cool the chamber walls by means of forced convection. The second option forgoes an active cooling system, and instead employs an ultra-high temperature ceramic (UHTC) in the construction of the chamber walls.

II.V.I Thermal Loading

The largest source of heat transfer to the engine walls is via forced convection, with radiation also accounting for up to 40 % of heat transfer in the combustion chamber.

Convective heat transfer coefficients are generally calculated by means of a Nusselt number correlation. The Dittus-Boelter relation (eq. [24]) is used here. This relation can estimate the heat transfer coefficient implicitly, without requiring knowledge of the wall temperature.

$$h = 0.026\left(\frac{\rho u d}{\mu}\right)^{0.8}\left(\frac{\mu c_p}{k}\right)^{0.4} \qquad [24]$$

Radiation heat transfer from combusting gases has been shown to be caused predominantly by H_2O and CO_2[7]. In order to estimate the total emittance of these two gases to the chamber walls, the Mean Beam Length method is employed. This method is based on experimental results, and uses a combination of pressure, temperature and enclosure size to predict the emittance of a hot gas to its surroundings. Charts used to predict the emittance of the gas can be found in NASA SP-164[9].

Both the convective and radiative heat transfer are dependent on values which vary throughout the engine. As such, in order to analyse the thermal response of the thrust chamber accurately it is necessary to split the wall into a finite number of elements, and calculate the heat transfer at each point.

II.V.II Regenerative Cooling

In the regeneratively cooled rocket engine, the oxidiser is passed over the outside of the thrust chamber before being injected into the engine. This serves to cool the chamber walls by means of forced convection. This is a fairly common method of cooling thrust chambers, as the heat rejected through the walls of the chamber results in an increase in temperature of the oxidiser, which can serve to increase combustion efficiency.

It is noted that during the low thrust operation of this engine, only a fraction of the typical oxidiser flow rate is available. This means that the geometry of the system must be designed to be able to appropriately cool both the high and low thrust cases.

Once more, the Dittus-Boelter relation can be used to assess the convective heat transfer coefficient in the coolant channels, however as heat is being transferred into rather than out of the fluid, the final power in eq. [24] should be changed to 0.33.

In order to produce an initial size for the cooling channels, a steady state energy balance was taken around the throat region, as identified in Figure 5. By specifying an inner wall temperature less than the maximum service temperature of the materials being used, and a wall thickness (initially estimated as 1 mm), the equations could be solved for a required channel height and width.
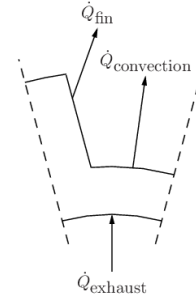

Figure 5: Depiction of thermal loading on a cross section of a coolant channel.

Once the coolant channels had been sized for the throat, consideration then had to be paid as to how these dimensions would vary throughout the chamber. It was decided to maintain a constant coolant channel height, but allow the width of the channels to increase with the circumference of the chamber. This would allow for a more even circumferential temperature distribution, lower coolant channel pressure drop, and reduced mass compared to constant dimension channels.

Typically, alloys with high copper content are used in the construction of rocket engines, as their high conductivity allows for a relatively low temperature difference across the inner wall. Unfortunately, copper and hydrogen peroxide are not compatible with one another, therefor materials with a high copper content could not be considered for this engine.

Two alternative materials were considered for use: Stainless Steel 316, due to its noted compatibility with hydrogen peroxide; and Inconel 718, a nickel-based superalloy known to have excellent high temperature mechanical properties. Some properties of these materials are given in Table 3.

Property		Stainless Steel 316	Inconel 718
σ_{UTS} (MPa)	300 K	579	1432
	1200 K	108	353
E (GPa)	300 K	193	211
	1200 K	123	148
k (W/m²K)	300 K	13.4	11.4
	1200 K	27.1	25.9

Table 3: Selection of properties for Stainless Steel 316[1] and Inconel 718[10].

In order to obtain an accurate representation of the steady state response of the thrust chamber, a full 3D finite element analysis was performed in ANSYS. First the calculated thermal loading was applied to acquire the correct temperature distribution, before a structural analysis was performed based on the
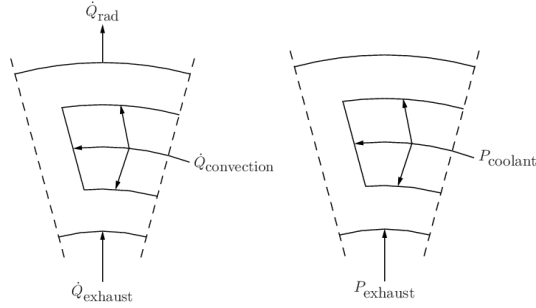
Figure 6: Loading on thermal and structural ANSYS models.

internal pressures and calculated temperatures. Figure 6 shows the loading and symmetry conditions applied to the model. In both cases, material properties were modelled to be temperature dependant.

II.V.III Radiation Cooling

For the propellants and mixture ratio being employed in the engine, the combustion temperature is expected to be 2877 K. If a material were to be used with a melting point higher than this temperature, there would be no need for an active cooling system to prevent thermal failure. This is important as it would reduce mass compared to the piping and pumping requirements of a regenerative system, as well as reducing engine complexity.

A family of materials meeting this criterion are Ultra-High Temperature Ceramics. These materials are diborides, carbides and nitrides based on the transition metals, and have extremely high melting points, as shown in Table 4.

Material	Melting Point (K)
HfB_2	3653
HfC	4173
HfN	3658
ZrB_2	3518
ZrC	3673
ZrN	3223

Table 4: Selection of UHTCs and their melting points[5].

Two UHTC based materials are analysed, with their material properties given in Table 5.

Property	ZrB_2/SiC/$TaSi_2$	HfB_2/SiC/$TaSi_2$
σ_y (MPa)	864	1055
E (GPa)	133	178
k (W/m^{2}K)	32.5	27.5
α (10^{-6}K^{-1})	7.5	8.75
ρ (kg/m^3)	5950	9090

Table 5: Selection of properties for UHTCs at 1423 K[5].

For an uncooled engine, the steady state operating condition is not necessarily the highest stress condition. Whilst the internal pressures are likely to be a maximum, the outer and inner surfaces will be at a similar temperature, meaning they will expand in a similar manner, and thus stresses as a result of differing thermal expansion will be low.

Conversely, during start-up, the difference in temperature across the chamber wall may be significant, and thus there may be significant stresses as a result of differing thermal expansion. This is known as thermal shock, and the stresses due to convective thermal shock can be calculated using eq. [25][6].

$$\sigma = \frac{Ea\Delta T}{(1-v)}\frac{ht}{2k} \qquad [25]$$

In rocket engines, due to the high amount of heat transfer, the critical design condition is the throat. Using the heat transfer coefficient and temperature associated with the throat, the stresses due to thermal shock were calculated for different materials at various thicknesses. These were then combined with the hoop stresses caused by the internal pressure, given by eq. [26], to give total stresses. Values for mechanical and thermal properties in these equations were taken as the values at the mid-temperature of the shock.

$$\sigma = \frac{pr}{t} \qquad [26]$$

To analyse the steady state condition, a finite element model similar to that in section II.V.II was created.
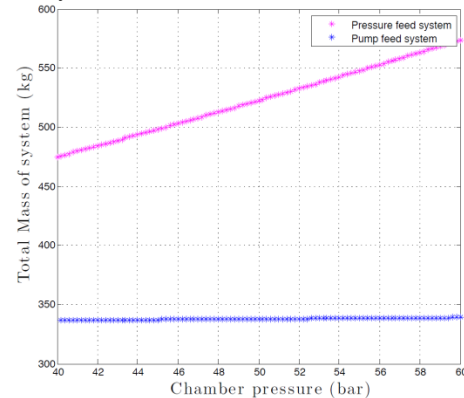
III. RESULTS
III.I Feed System

Figure 7: Mass comparison of pump and pressure fed systems with changes in chamber pressure.

Figure 7 shows the results of the mass estimation for the pump and pressure fed systems over a range of chamber pressures.

It is clear that for the range of pressures relevant to the design of this engine, the pump fed system is far superior to the pressure fed system in terms of saving mass.

Table 6 shows the calculated pump and turbine power requirements, as well as the required gas generator mass flow rate for both the cases with and without regenerative cooling. It can be seen that despite the losses associated with travelling through the cooling passages, the presence of a regenerative cooling system does not have a large effect on the required gas generator mass flow rate.

Case	Fuel Pump Power (W)	Ox. Pump Power (W)	Turbine Power (W)	Gas Gen. Mass Flow (kg/s)
No Regen. Cooling	2382	8655	13796	0.0175
Regen. Cooling	2382	8669	13814	0.0176

Table 6: Nominal flight system parameters

III.II Injection System

Figure 8 shows results from the CFD analysis performed to compare the various injector designs.
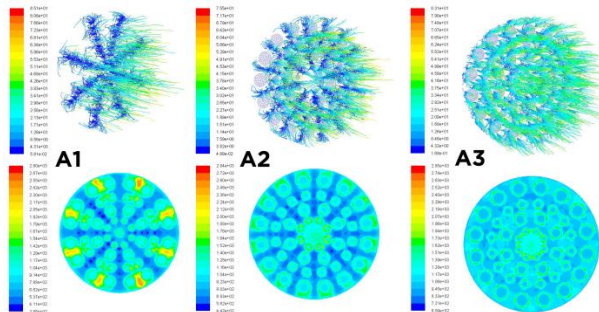

Figure 8: Results from the CFD analysis for the various injector designs. First row shows liquid kerosene particle traces coloured by velocity. Second row shows static temperature 2 mm from injector face.

It can be seen that injector design A3 both allows the fuel to flow more evenly throughout the chamber, and for a more even static temperature distribution. This implies that the fuel and oxidiser are mixed more efficiently, allowing for a more complete combustion.

Figure 9 confirms this, showing that when the final nozzle design was incorporated into the model,

the predicted thrust from the engine using injector A3 was greatest, at almost 103 % of the desired 5000 N.
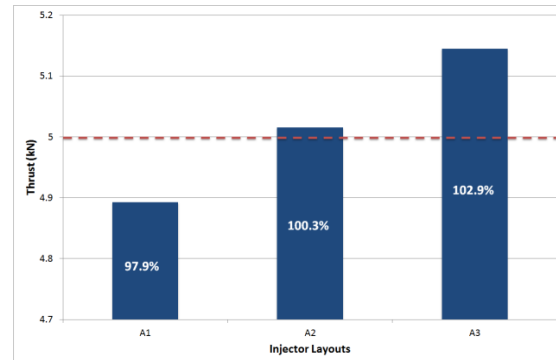

Figure 9: Measured thrust from CFD model incorporating final nozzle design.

III.III Combustion Chamber

Results from the CFD model are shown in Table 7 and Table 8. It can be seen that increasing characteristic length increases predicted thrust. The same was not true for the area ratio (of the chamber to the throat) which produced a peak thrust at a value of 11.

L^* (m)	p_1 (bar)	v_2 (m/s)	c^* eff. (%)	Thrust (N)
1	44.6	2299	97.0	4720
1.25	44.5	2313	96.6	4747
1.5	45.1	2327	98.0	4777

Table 7: Combustion chamber results for fixed area ratio of 9. Injector A0 was the control for this analysis.

Area ratio	p_1 (bar)	v_2 (m/s)	c^* eff. (%)	Thrust (N)
9	44.5	2312	96.6	4747
11	43.5	2387	94.4	4901
13	42.1	2323	91.6	4769

Table 8: Combustion chamber results for fixed $L^* = 1.25$. Injector A0 was the control for this analysis.

III.IV Nozzle

The trajectory simulation of different nozzle design conditions (Figure 10) showed that propellant usage decreased for design conditions higher than sea level, providing a reason to launch over-expanded. It is of note that the optimal design altitude is at risk of flow separation on launch due to the 25 to 40 % exit pressure mentioned previously. Most rocket nozzles do not have to land however, and those that do[*]

[*] SpaceX Falcon 9 v1.1 first stage

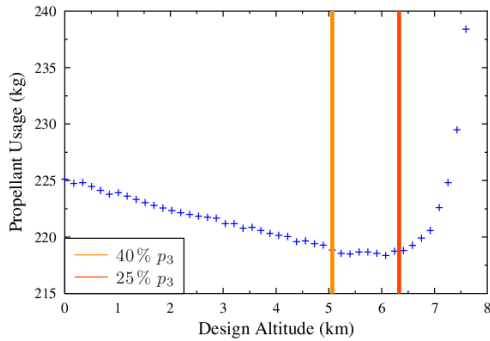typically have multiple engines and throttle by shutting down some engines.

Figure 10: Propellant usage of nozzles with different design altitudes.

Figure 11 shows the relationship between flight conditions and stagnation pressure. It is clear that at lower altitudes—e.g. when landing—the stagnation pressure is likely to be a problem and therefore velocity limits will need to be provided to ensure the engine performs as expected. For this reason, a nozzle with a design altitude greater than sea level would severely compromise the performance of the rocket during landing. A design altitude of sea level is then chosen for the nozzle.
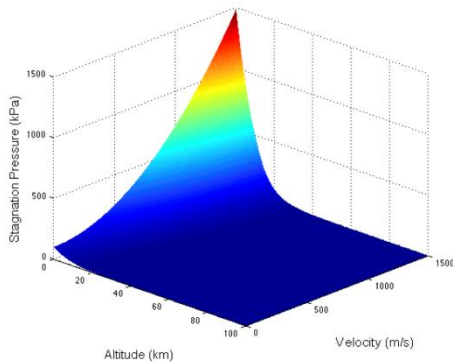

Figure 11: Stagnation pressure as a function of altitude and velocity.

To compensate for real nozzle performance with the ideal design, a total thrust efficiency of 86 % was assumed.

The final nozzle geometry was determined using the calculations outlined in section II.IV.III. The dimensions are shown in Table 9 for Figure 12.
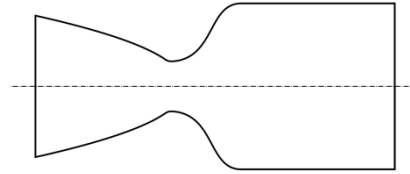

Figure 12: Accurate representation of final combustion chamber and nozzle geometry.

Property	Symbol	Dimension	Unit
Length (throat to exit)	L	82.9	mm
Throat radius	r_t	15.2	mm
Exit radius	r_2	43.0	mm
Inflection angle	θ_n	34.6	deg
Exit angle	α	6.3	deg

Table 9: Final nozzle geometry. Shape profile: optimal Rao bell.

III.IV.I Performance
The designed rocket nozzle has the performance characteristics outlined in Table 10.

Property	Symbol	Value	
Specific impulse	I_{sp}	266.1	s
Mass flow rate (full thrust)	$\dot{m}$	2.21	kg/s
Mass flow rate (800 N)	$\dot{m}$	0.55	kg/s
Ideal Thrust	F	5772	N
Exit velocity	v_2	2610.3	m/s
Exit Mach number	Ma_2	2.95	
Real thrust (predicted)	F_{real}	5000	N

Table 10: Final nozzle performance. Note that I_{sp}, v_2, and Ma_2 will have different values in reality due to the mentioned losses.

III.IV.II Operating Conditions
The flow conditions inside the nozzle at full throttle are given in Table 3.

Property	Symbol	Value	
Throat pressure	p_t	2.893	MPa
Exit (design) pressure	p_2	101.325	kPa
Throat temperature	T_t	2703	K
Exit temperature	T_2	1842	K

Table 11: Operating conditions at full throttle.

III.IV.III Throttling

Evaluating the nozzle for the throttling methods mentioned in section II.IV.V, it was found that the standard propellant mix ratio with the reduced mass flow rate provided the largest thrust range as shown by Figure 13 and Figure 14.
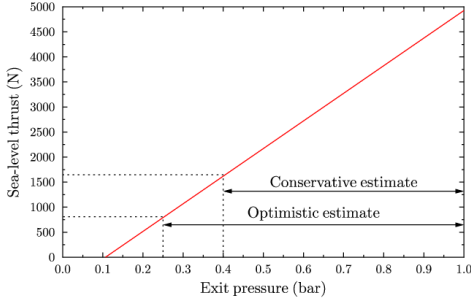

Figure 13: Estimation of throttle range for standard propellant. Flow separation is likely to occur somewhere between the conservative and optimistic estimates, giving a thrust range of anywhere from 809 N or 1648 N up to 5 kN.
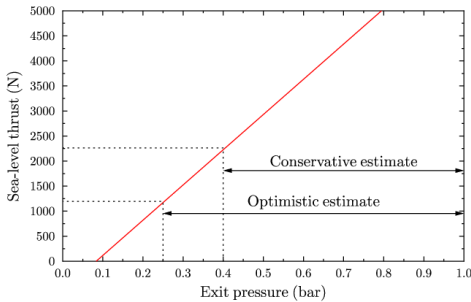

Figure 14: Estimation of throttle range for oxidiser only. Flow separation is likely to occur somewhere the conservative and optimistic estimates, giving a thrust range of anywhere from 1194 N or 2263 N up to 5146 N.

Throttling, of course, is mainly a requirement for descent and landing. As discussed previously, there are stagnation pressure limits in order that flow separation does not occur. The velocity limits as a function of altitude and thrust are shown in Figure 15 and Figure 16. It is clear that the descent requirement has severe implications on the engine design. The engine has to deal with pressures much higher than atmospheric pressure at sea level, despite launching into a decreasingly pressurised atmosphere.

For a given thrust level, there is an altitude-dependent velocity limit above which flow separation is likely to occur where performance becomes increasingly inefficient. The most important limit is that of the maximum thrust case, above which deceleration may not be possible.
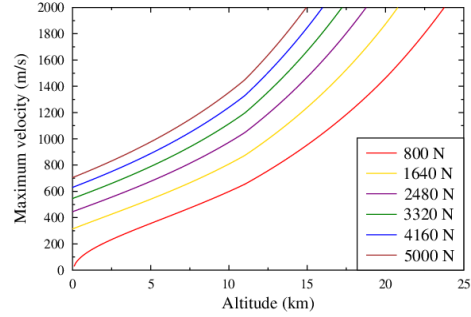

Figure 15: Optimistic stagnation pressure limits as a function of altitude, velocity, and thrust level.
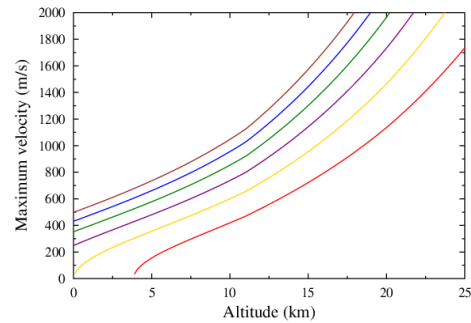

Figure 16: Conservative stagnation pressure limits as a function of altitude, velocity, and thrust level.

III.V Thermal Control System
III.V.I Thermal Loading

Figure 17 shows a comparison of the radiative and convective heat fluxes in the high thrust case. Through the majority of the thrust chamber, the convective heat flux significantly dwarfs the radiative heat flux. However, this is not the case in the combustion chamber, where the two are almost equal. This would indicate that the radiative heat flux has
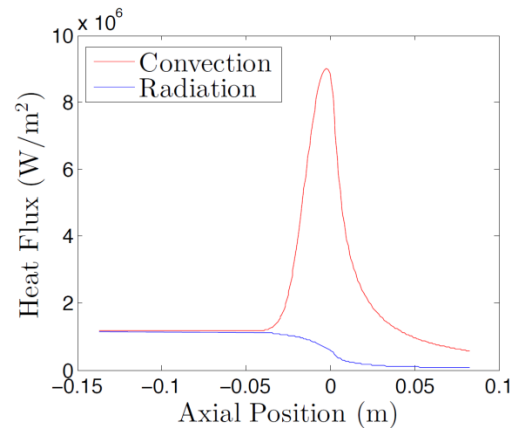

Figure 17: Predicted heat flux due to convection and radiation at a wall temperature of 1000 K.

been overestimated, as it is typically considered to be between 5 – 40 % of the convective heat flux.

III.V.II Regenerative Cooling

The results from the energy balanced use to determine the coolant channel dimensions at the throat are shown in Table 12. These are designed to maintain an exhaust side wall temperature of 1000 K.

No. of Channels	Width (mm)	Height (mm)
40	1	1
20	2	1

Table 12: Initial cooling channel geometries at throat.

The FEA results corresponding to the 40-channel geometry are given in Table 13 and Table 14.

Inner Wall Thickness (mm)	Exhaust Side Wall Temp. (K)	Coolant Side Wall Temp. (K)	Stress at Throat (MPa)	Mass (kg)
1.00	944.9	413	1700	1.056
0.50	769.3	423	1350	0.809
0.40	743.5	423	1130	0.760

Table 13: FEA results for Stainless Steel 316 (40-channel)

Inner Wall Thickness (mm)	Exhaust Side Wall Temp. (K)	Coolant Side Wall Temp. (K)	Stress at Throat (MPa)	Mass (kg)
1.00	984.4	415	1710	1.086
0.50	806.4	412	1250	0.832
0.40	778.4	417	1150	0.782

Table 14: FEA results for Inconel 718 (40-channel)

It is clear that whilst the thermal environment was close to that which was expected, there were unacceptable stress levels for the case of 1 mm wall thickness. These stresses were largely the result of extremely high temperature differentials across the inner wall of the chamber. In order to reduce these stresses, it was then necessary to reduce the temperature difference, by decreasing the wall thickness. At a wall thickness of 0.4 mm, the Inconel 718 chamber design becomes viable from both a structural and thermal standpoint.

Results corresponding to the twenty channel geometry are given in Table 15.

No. of Channels	Exhaust Side Wall Temp. (K)	Coolant Side Wall Temp. (K)	Stress at Throat (MPa)	Mass (kg)
40	778.4	417	1150	0.782
20	915.7	414	1590	0.779

Table 15: Effect of changing number of coolant channels (Inconel 718, Wall Thickness 0.4 mm)

This design did not perform as well as the original. Due to the relatively low thermal conductivity of the materials being used, the cooling effect of the channels is localised. This caused a large temperature increase in the areas between the channels, resulting in higher thermal stresses. The temperature variation is illustrated by Figure 18.
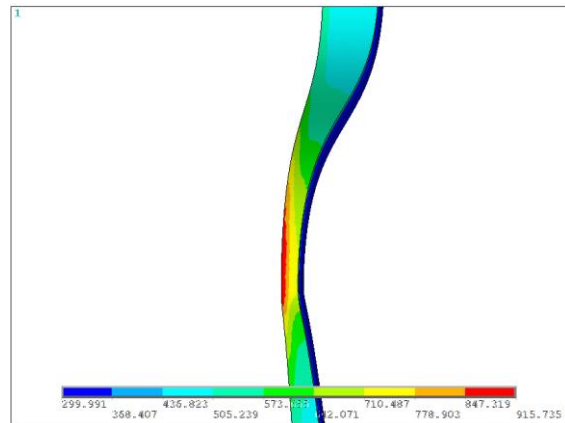

Figure 18: Temperature increase between coolant channels at throat region.

The performance of the system in the low thrust case was also considered. It can be seen from Table 16 that both the stresses and wall temperatures are much lower in this case, indicating that the design conditions for the high thrust case completely envelope those of the low thrust case.

Thrust Case (N)	Exhaust Side Wall Temp. (K)	Coolant Side Wall Temp. (K)	Stress at Throat (MPa)
5000	778.4	417	1150
800	501.9	413	568

Table 16: Performance in low and high thrust cases (Inconel 718, Wall Thickness 0.4 mm)

III.V.III Radiation Cooling

For a variety of wall thicknesses, the associated stresses for the radiation cooled chamber designs are given in Table 17 and Table 18.

Wall Thick (mm)	Thermal Shock Analysis Stresses (MPa)			Steady State Analysis / FEA	
	Therm. Stress	Hoop Stress	Total Stress	Stress (MPa)	Mass (kg)
0.50	358.4	83.9	442.3	652	0.177
0.75	537.6	55.9	593.5	419	0.265
1.00	716.8	41.9	758.8	309	0.355
1.25	896.0	33.5	929.6	243	0.445
1.50	1075.2	28.0	1103.2	202	0.535

Table 17: FEA results for $ZrB_2/SiC/TaSi_2$

Wall Thick (mm)	Thermal Shock Analysis Stresses (MPa)			Steady State Analysis / FEA	
	Therm. Stress	Hoop Stress	Total Stress	Stress (MPa)	Mass (kg)
0.50	494.1	83.9	578.0	653	0.271
0.75	741.2	55.9	797.1	420	0.405
1.00	988.3	41.9	1030.2	310	0.542
1.25	1235.3	33.5	1268.9	244	0.679
1.50	1482.4	28.0	1510.4	203	0.818

Table 18: FEA results for $HfB_2/SiC/TaSi_2$

It is clear that there are competing requirements on the design: during the thermal shock process a thinner chamber wall is more desirable to reduce the temperature differential, whereas during the steady state operation, a thicker wall is desirable to withstand the internal pressures. For both of the materials analysed, the largest value of wall thickness capable of withstanding the thermal shock was 1 mm. This corresponds to a steady state stress of 310 MPa, which neither of the materials are capable of withstanding at the associated temperatures.

It is noted that the masses calculated for the radiation cooled chambers are lower than those of the regeneratively cooled chambers calculated in section III.V.II. This indicates that if the material properties of UHTCs could be improved at high temperatures, they would be able to provide a respectable system mass reduction.

IV. CONCLUSION

A rocket propulsion system design has been composed which satisfies the design requirements of the client. It is predicted to deliver up to 5150 N of thrust at take-off and is capable of throttling down to somewhere in the range of 800 – 1600 N before flow separation occurs. The design has been optimised to reduce mass and increase performance, and the engine has been designed to be structurally sound through all phases of flight.

The final design consists of a gas generator powered pump feed system, a nozzle optimised for performance at sea-level and a regenerative cooling system.

CFD and FEA models have been used where possible in order to accurately optimise the design of complex systems, and consideration has been given to the unique flight environment in which the launch vehicle will operate.

Further design improvements could be made by performing a more detailed investigation into the mechanical properties of ultra-high temperature ceramics at ultra-high temperatures, or by developing a better understanding of precisely when flow separation begins to occur in this rocket design.

V. BIBLIOGRAPHY

[1] American Iron and Steel Institute. High-temperature characteristics of stainless steels.

[2] D. Andrews and H. Sunley. The gamma rocket engines for black knight. *British Interplanetary Society*, 43:301–310, July 1990.

[3] Callum Harrower. CFD Modelling of Combustion Process in a Bipropellant Liquid Rocket Engine: Initial Combustion Chamber Design, Optimisation and Validation. April 2014.

[4] Sungkwon Jo, Sungyong An, Jonghak Kim, Hosung Yoon, and Sejin Kwon. Performance characteristics of hydrogen peroxide/kerosene staged-bipropellant engine with axial fuel injector. *Journal of Propulsion and Power*, 27(3):684–691, May 2011.

[5] J.F. Justin and A Jankowiak. Ultra high temperature ceramics: Densification, properties and thermal stability. *Aerospace Lab*, 3, November 2011.

[6] National Physical Laboratory. *Handbook of Properties of Technical and Engineering Ceramics: An Introduction for the Engineer and Designer Pt. 1*. Stationery Office Books, 1985.

[7] William Henry McAdams. *Heat Transmission*. Krieger Pub Co, 1985.

[8] G. V R. Rao. Recent developments in rocket nozzle configurations. *ARS Journal*, 31(11):1488–1494, Nov 1961.

[9] John Siegel and John R. Howell. Radiation transfer with absorbing, emitting, and scattering media. *Thermal Radiation Heat Transfer*, 3, 1971.

[10] Special Metals Corperation. Inconel 718 Data Sheet. September 2007.

[11] George P. Sutton and Oscar Biblarz. *Rocket Propulsion Elements, 7th Edition*. Wiley-Interscience, 2000.

[12] Viriato Semiao, Pedro Andrade, Maria da Graca Carvalho. Spray characterization: numerical prediction of Sauter mean diameter and droplet size distribution. *Fuel*, 75(15):1707–1714, May 1996.